ADVANCED MATERIALS
www.advmat.de

Embedded 3D Printing of Multimaterial Polymer Lattices via Graph-Based Print Path Planning

*Robert D. Weeks, Ryan L. Truby, Sebastien G. M. Uzel, and Jennifer A. Lewis**

Recent advances in computational design and 3D printing enable the fabrication of polymer lattices with high strength-to-weight ratio and tailored mechanics. To date, 3D lattices composed of monolithic materials have primarily been constructed due to limitations associated with most commercial 3D printing platforms. Here, freeform fabrication of multi-material polymer lattices via embedded three-dimensional (EMB3D) printing is demonstrated. An algorithm is developed first that generates print paths for each target lattice based on graph theory. The effects of ink rheology on filamentary printing and the effects of the print path on resultant mechanical properties are then investigated. By co-printing multiple materials with different mechanical properties, a broad range of periodic and stochastic lattices with tailored mechanical responses can be realized opening new avenues for constructing architected matter.

1. Introduction

Precise control over material composition and geometry enables the design of high-performance architectures with exotic mechanical properties.[1–3] Several recent advances have been reported, including ultralight lattices,[4–7] novel auxetics,[8,9] spatially and thermally programmable mechanical behavior,[10–13] shape-reconfigurable structures,[14–20] and multi-stable buckling for energy trapping and mechanical logic.[21,22] While architected materials may find potential application in aerospace, robotics, structural engineering, and well beyond,[1,23–25] challenges remain in the scalable fabrication of complex, multi-material 3D structures with arbitrarily programmed composition and performance.

The integration of computational design[12,14,26–30] with digital fabrication[31,32] has vastly accelerated interest in architected matter. Both light and ink-based 3D printing methods have been used to produce such structures. However, each digital fabrication method has inherent limitations. For example, stereolithography (SLA), digital projection lithography (DLP),[12,33–39] two-photon polymerization (2PP),[4,6,7,18,20,40] and selective laser sintering (SLS)[41–45] enable the construction of high-resolution, 3D architectures, but they are typically limited to patterning a single material using photopolymer resins or powder beds. While progress has been made toward multi-material SLA and DLP printing,[33,46] including voxel-level control of mechanical properties via magnetic control over short fiber orientation,[47] these methods remain limited to photopolymerizable resins. By contrast, direct ink writing (DIW)[11,17,19,21,22,26,48–51] enables fabrication of architected lattices from the broadest array of materials, including ceramics,[48,49] elastomers,[26] epoxy resins,[11,50] and multi-material composites.[17,51,52] However, this method is confined to layer-by-layer fabrication of simple lattices, such as woodpile structures.

Here, we report a method for fabricating periodic and stochastic architected lattices via embedded 3D (EMB3D) printing[53–59] with spatially controlled composition and mechanical properties. Print path generation is central to our free-form printing strategy. While periodic lattices can be printed using semi-manual print path generation methods, we developed a graph theory-based algorithm, termed Automated Eulerian Route Optimization (AERO), to automate the printing of stochastic lattices with hundreds of struts. Next, we created epoxy resin-based inks that exhibit a viscoelastic response, enabling extrusion through a nozzle translated omnidirectionally within a shear-thinning, yield-stress matrix material composed of a granular silicone microgel. We tailored the ink and matrix material rheology to ensure high-fidelity EMB3D printing and designed each material to facilitate retrieval and post-processing of the printed lattices. Building on our recent work,[60] we investigated the impact of print path design and part orientation on their shape fidelity and mechanical behavior. To date, mechanical property measurements have only been reported for simple cylinders (or strips) composed of hydrogels and PDMS printed and removed from their respective supporting matrices.[55,61–65] Finally, we used the insights gained to generate multi-material, periodic lattices with programmable mechanical responses as well as complex stochastic lattices. Our integrated platform for fabricating architected lattices opens new avenues for creating lightweight composites and mechanical metamaterials.

R. D. Weeks, R. L. Truby, S. G. M. Uzel, J. A. Lewis
John A. Paulson School of Engineering and Applied Sciences
Harvard University
Cambridge, MA 02138, USA
E-mail: jalewis@seas.harvard.edu
S. G. M. Uzel, J. A. Lewis
Wyss Institute for Biologically Inspired Engineering
Harvard University
Cambridge, MA 02138, USA
The ORCID identification number(s) for the author(s) of this article can be found under https://doi.org/10.1002/adma.202206958.

DOI: 10.1002/adma.202206958

2. Results and Discussion

EMB3D printing of architected lattices requires the co-design of appropriate print paths, inks, and matrix materials. A representative build sequence for constructing complex 3D lattices via EMB3D printing is shown in **Figure 1**a. Lattices are printed in the matrix with a bottom-up approach using a print path that avoids nozzle translation through previously deposited ink filaments. Lattices are cured within the matrix and then removed for subsequent cleaning and characterization. For lattices with repeating unit cells, a semi-manual approach is developed to create the print path by manually designing the path to traverse a single unit and extrapolating it to an arbitrary number of cells using a parameterized framework. Since each print path must be individually designed, this approach is only suitable for periodic lattices. To create lattices of arbitrary geometry, we used our AERO algorithm to efficiently generate their print paths. This method is necessary in part, because manual (point-by-point) designs[53] are impractical for stochastic lattices composed of hundreds of struts. These architectures are also not well represented by analytical 3D functions[56,66] and slicing software[55,61,67–72] splits every strut into small layers instead of directly printing a given filament in 3D.

In EMB3D printing, the nozzle is translated through a supporting matrix that facilitates the omnidirectional printing of one or more inks. Ideally, these ink(s) are continuously printed until the 3D object is fully fabricated. However, in practice, the topology of the structure usually requires a print path to include nozzle motions without ink extrusion, termed travel motions, to realize a given design. To prevent disruption of printed features, the nozzle can be retracted vertically out of the matrix, then translated in the x-y plane to the next location before reentering the matrix to the required depth to print the next feature. To reduce build times, our AERO algorithm seeks to minimize the number of travel motions both within and outside of the matrix during EMB3D printing. Additionally, one must generate print paths that avoid collisions between the nozzle and previously printed features as well as allow for switching between different nozzles when multiple materials are co-printed. Although applied to EMB3D printing in this context, AERO can be used as a general path planner for DIW. An example of AERO print path for a flat 2D truss structure in shown in Movie S1 (Supporting Information).

AERO is used to determine an optimal print path for each lattice. The geometry of any lattice can be concisely defined as a graph using an ordered list of vertex coordinates (x,y,z) and an unordered list of edges (n_1,n_2), that define an element connecting two vertices. A graph can be either directed, undirected, or mixed (Figure S1, Supporting Information). In an undirected graph, the edges can be traversed in either direction whereas, in a directed graph, edges can only be traversed in a single direction. An mixed graph contains both types of edges. From the list of edges, a graph representing the topology of the lattice can be constructed. The goal is then to find a path to traverse all edges in the graph. This is analogous to the path the nozzle makes during EMB3D printing, which must pass through each strut only once. Struts within a ≈30° cone surrounding the nozzle axis should be printed from the bottom-up to prevent collision with the nozzle (Figure S2a, Supporting Information). This can be easily understood in the case of a vertical strut. If printed top-down, the nozzle would traverse directly through the ink being deposited resulting in a failed print. Thus, edges within the graph can be directed and must be traversed as such. Given the 3-axis robotic system used, only a subset of the struts in the lattice can be printed at a time without blocking access to the printing of future struts. Without taking this into account, the nozzle could interfere with an already printed strut when printing a new strut (Figure S2b, Supporting Information). For the case of an octet lattice, the geometry does not require directed edges. The corresponding graph for the octet unit cell shown in Figure 1b, with 14 vertices and 36 edges is shown in Figure S3 (Supporting Information).

Any lattice can be broken into sequential groups of struts, such that collisions between the nozzle and an already printed strut in another group will not occur if the groups are printed in the correct order. Furthermore, by definition, struts within each of these groups can be printed in any order without the possibility of collisions. Groups are formed by iterating over all the struts in a lattice, to see if the printing of each strut would interfere with the future printing of any other struts. If a strut can be printed such that the rest of the struts are still accessible to be printed later, thus avoiding future collisions, it is marked as valid (Figure S4, Supporting Information). The validity of a strut is determined by comparing the position of a line segment representing the strut to all the line segments for the other struts in the design. Once all the valid edges in a lattice are determined they can be combined to form a group; the group is then removed from the lattice. The process is then repeated until every strut is assigned a group (Movie S2, Supporting Information). The three groups for an octet unit cell are shown in Figure 1b, in which each group corresponds to an equivalent subgraph of the larger graph representing the entire lattice. We can then find paths to traverse the subgraph corresponding to each individual group and concatenate them to form a print path for the entire lattice. The minimum number of paths to traverse all edges in a graph is dependent on its topology.

In graph theory, an Eulerian path is a traversal through a graph visiting every edge exactly once, though vertices can be visited multiple times.[73] The degree of a vertex in a graph is the number of edges incident to it. If the degree of all vertices in an undirected graph is even, it contains an Eulerian circuit, such that starting on any vertex, there exists a path that traverses every edge in the graph and returns to the initial starting point. The term Eulerian graph is used to denote a graph with an Eulerian circuit. If the degree of vertices in an undirected graph is not all even, the number of vertices of odd degrees will always be even. We know this to be true as the sum of the degrees of all the vertices equals twice the number of edges in an undirected graph. In the special case of a connected undirected graph with all but two vertices of even degree, it contains an Eulerian path beginning and ending on a couple of odd-degree vertices. This type of graph is called semi-Eulerian. Fleury's algorithm is a simple, but elegant process to determine Eulerian circuits or paths to traverse a graph (Figure S5, Supporting Information).[74] We have found that successive applications of Fleury's algorithm to non-Eulerian graphs will generate paths partially traversing the graph, which when combined form a series of paths that traverse the entire graph

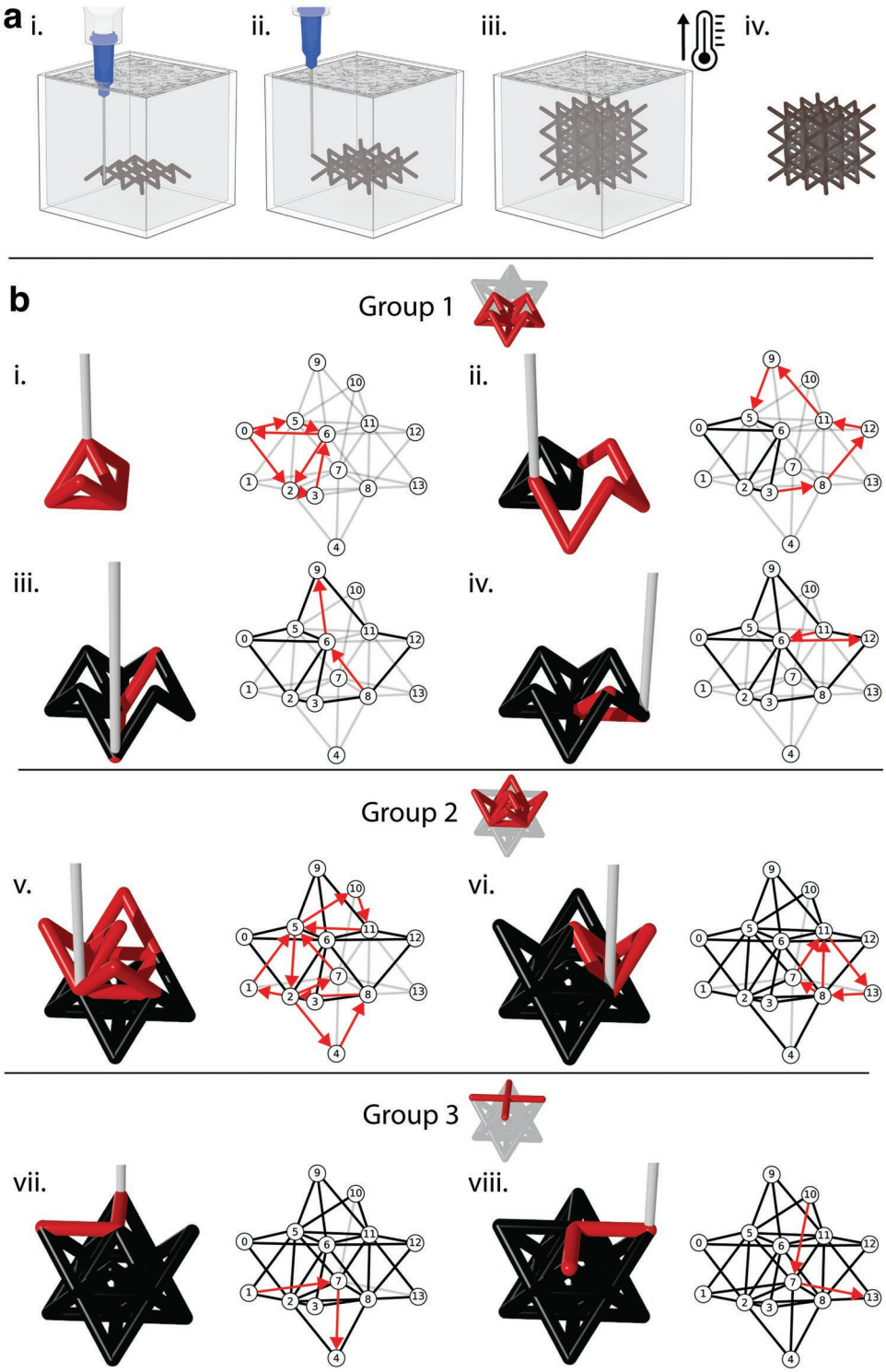

Figure 1. Embedded 3D printing of architected lattices via graph-based print path planning. a) Schematic illustration of embedded 3D printing of a periodic lattice: i) print first layer of struts, ii) repeat printing in layerwise manner until completion, iii) cure lattice in matrix, iv) remove and clean part. b) Automated Eulerian Route Optimization (AERO) for generating the print path for an octet unit cell. The left side of each frame shows the progression of printing an octet unit cell in 8 steps (i-viii). The right side of each frame shows the corresponding nozzle motion during that step in the graph representation of the lattice. Each vertex in the graph is labeled with an index, corresponding to a vertex on the lattice. The grey lines represent struts that have not yet been printed, the red lines show the print path during the current step, and the black lines represent lines that have been completed.

(Figure 1b). Fleury's algorithm always starts with an odd degree vertex, resulting in a path ending on another odd degree vertex, or if none exists an even degree vertex is used resulting in an Eulerian circuit. If the edges in the resulting path are removed from the graph the two odd degree vertices will lose an incident edge and become even or be removed if it was their only incident edge. Furthermore, since the path goes in and then out of every vertex along it, every other vertex will lose two degrees and maintain the same state of even or odd. Thus, the removal of the path will always remove a couple of the odd (degree) vertices. Because of this, an undirected graph can be split into a minimum of $n/2$ continuous trails with n being the number of odd (degree) vertices. This approach to finding a series of paths to traverse a graph also works on mixed graphs, if Fleury's algorithm is initiated on vertices with an odd out-degree. Importantly, the resulting print for the octet unit cell using AERO has completed 8 steps compared to the 18 steps required using our semi-manual approach (Figure 1b, Movie S3, Supporting Information). By iterating over the list of paths output from AERO and adding travel motions between paths, a route for printing the entire strut-based structure can be generated. The resulting print paths from each approach for a $3 \times 3 \times 3$ octet lattice are shown in Movie S4 (Supporting Information) and quantitatively compared in Figure S6 (Supporting Information). Notably, AERO consistently requires less travel motions than the semi-manual approach largely due to the presence of much longer paths, encompassing up to 35 edges, in the former case. When testing the printing routes generated by AERO, we find that some edges fail to properly connect to form a node (Figure S7a, Supporting Information). This can occur when printed features are pushed away by a yield region around the incoming nozzle when connecting to a node.[60] To remedy this issue, the degree of overlap at the nodes in the print path can be tuned (Figure S7b,c, Supporting Information). AERO can also be implemented for print path planning of more complex structures, such as those based on multi-material and interpenetrating architectures. Each material or disconnected part must simply be represented as disconnected subgraphs during graph construction (Figure S8, Supporting Information).

Beyond print path optimization, EMB3D printing requires the formulation of ink and matrix materials that meet several requirements. First, these materials must be chemically compatible to avoid adverse side reactions, swelling, or other interactions that compromise structural integrity or mechanical performance of the printed objects. Second, their rheological properties must be tailored to facilitate EMB3D printing to both minimize distortion of the printed filamentary features (or struts) and prevent the formation of defects, such as crevices, within the matrix that emerges behind the translating nozzle.[53–55,57,59,60,75] Finally, unlike cross-linkable matrices that are retained in the final EMB3D printed object,[53,54,57–59] a sacrificial matrix material[55,56] that facilitates easy retrieval is required for printing periodic and stochastic lattice architectures. To meet the above requirements, we co-developed chemically compatible, epoxy resin-based thermoset inks,[11,50] and a solvent-free, silicone microgel matrix.[56] To investigate the effects of ink rheology on printed feature fidelity, we prepared three epoxy-based inks by combining a base epoxy resin with fumed silica (FS) nanoparticles with varying filler content of 2.8, 5.7, and 13.3 wt.% as a rheological modifier, curing agents, reactive diluents, or other additives. In addition to these rigid epoxy inks, a flexible epoxy ink that contains an epoxy flexibilizer is also created for printing multi-material lattices.

Inks and matrix materials created for EMB3D printing are typically Herschel-Bulkley fluids that exhibit characteristic yield stress followed by shear-thinning behavior.[53,54,57,60] Appropriate matrix materials have been designed from thixotropic, viscoplastic fluids[54,57,58,60] to jammed viscoelastic fluids with moderate yield stresses to avoid defect (crevice) formation.[55,57,59] Our rigid epoxy-based inks and silicone matrix materials exhibit shear-thinning (**Figure 2**a) and viscoelastic (Figure 2b) behavior. The apparent viscosity of the rigid epoxy ink with the lowest filler content (2.8 wt.% fumed silica) is roughly one order of magnitude lower than that of the silicone matrix, while the epoxy ink with the highest filler content (13.3 wt.% fumed silica) is an order of magnitude higher over the measured range of shear rates. By adjusting the filler content to 5.7 wt.% fumed silica, we generated an epoxy ink that matches both the apparent viscosity and shear thinning response across this experimentally relevant window. Concomitantly, as the filler concentration is increased, these epoxy inks exhibit plateau storage moduli, G′, of $\approx 1.7 \times 10^2$ Pa, 1.4×10^3 Pa, and 2.5×10^4 Pa and shear yield stress, τ_y, values of 1.6×10^1 Pa, 3.6×10^2 Pa, and 3.0×10^3 Pa, respectively. The matrix material exhibits a G′ of $\approx 2.0 \times 10^3$ Pa and τ_y of 5.1×10^2 Pa, which is close to the values obtained for the epoxy ink with an optimized filler content of 5.7 wt.% fumed silica. The shear yield stress is reported as the applied stress at the crossover point defined by G′ = G″, for inks containing 5.7 wt.% and 13.3 wt.% fumed silica. Since there is no crossover point for the 2.8 wt.% fumed silica ink, the shear yield stress is defined as the applied stress where G′ is 90% of its plateau value.

Importantly, substantial differences between the ink and matrix rheology have a pronounced effect on their embedded printing behavior (Figure 2c). We directly observe ink extrusion from stationary nozzles (Figure 2c(i)), translating nozzles (Figure 2c(ii)), and views from below intersecting filaments (Figure 2c(iii) and Figure S9, Supporting Information) to understand how printed filament morphology varies when the apparent viscosity, η_{ink}, is much lower than, approximately equal to, or far higher than that of the matrix, η_{matrix}. When $\eta_{ink} \ll \eta_{matrix}$, the printed ink spreads beyond the desired filamentary form, resulting in a teardrop cross-section (Figure 2c(ii)). When $\eta_{ink} \gg \eta_{matrix}$, the printed ink does not remain in the desired location as the filament is dragged through the matrix by the translating nozzle. Under these conditions, the ink tunnels through the matrix when extruded from a stationary nozzle rather than forming spherical bodies, hindering the formation of a robust mechanical connection at the nodes (Figure 2c(i)). When η_{ink} is slightly above η_{matrix}, the printed filaments exhibit the desired circular cross-section.[76] When printing lattices, we prioritized the integrity of their nodes by matching $\eta_{ink} \approx \eta_{matrix}$, even though this results in filaments that are not perfectly round. Our observations are in good agreement with predictions from finite element modelling[77] as well as our prior heuristics for achieving high fidelity EMB3D printing, which revealed that printable inks must also exhibit G′ values that

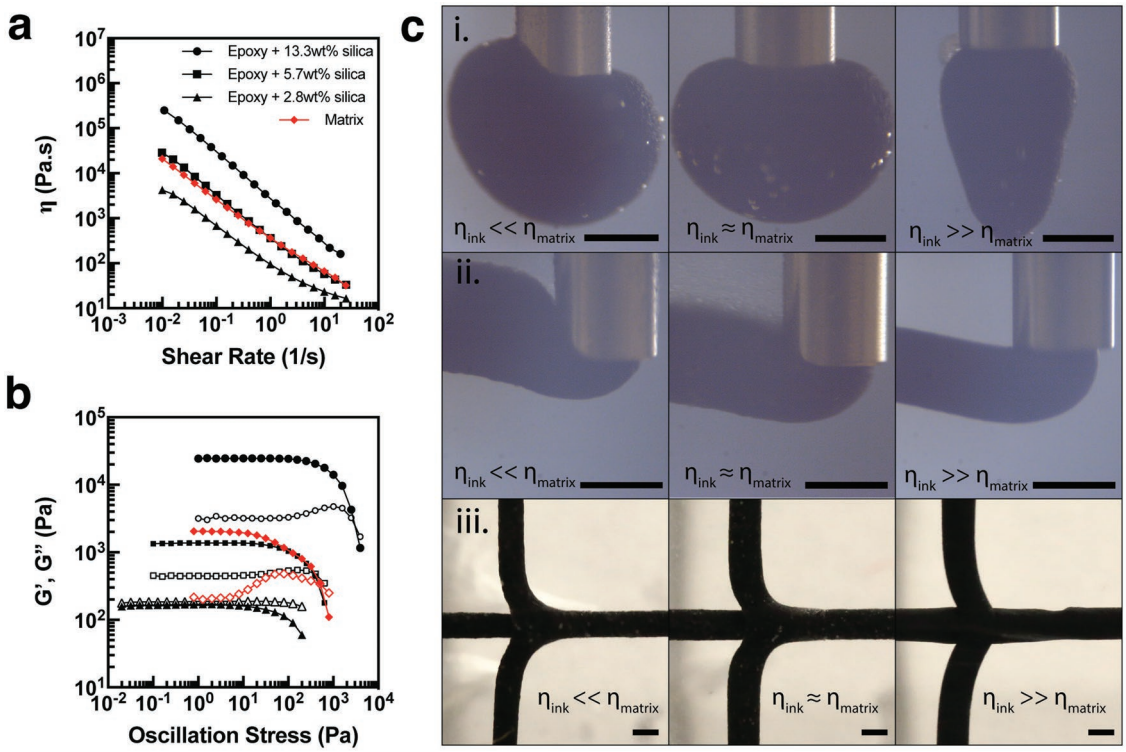

Figure 2. Ink, matrix rheology, and printing behavior during EMB3D printing. a) Apparent viscosity as a function of shear rate for epoxy inks with different fumed silica loadings and the granular silicone matrix. b) Log-log plot of the storage modulus, G' (filled symbols) and loss modulus, G" (unfilled symbols) as a function of shear stress for the same epoxy inks and matrix material. c) Localized flow behavior of inks at the nozzle exit during EMB3D printing, revealing the effects of viscosity differences between the ink and matrix materials, where i) resulting deposition following stationary extrusion for inks of varying viscosity compared to the matrix, ii) printed filament shape and position for inks of varying viscosity compared to the matrix, and iii) Images acquired from beneath a perpendicular filament printed across a previously printed filament in the same plane for inks with varying viscosities compared to the matrix. (scale bars = 1 mm)

are less than one order of magnitude higher than the matrix material.[54,57,59,60]

Figure 3a highlights representative examples of several lattice architectures that we produced by EMB3D printing using an epoxy ink with optimized rheology and semi-manual print paths (Movies S5–S9, Supporting Information), including body-centered cubic (BCC), cubic, diamond, octet, and dodecahedron lattices. We have previously demonstrated that the local yielding of the matrix material induced by nozzle translation during EMB3D printing can displace adjacent printed features.[60] Hence, we anticipate that the print path design will directly impact the fidelity of 3D objects fabricated by this method. Akin to other 3D printing methods,[78–81] the print path design and orientation may also impact the structural integrity and mechanical properties of EMB3D printed lattices. To explore these effects, we printed BCC lattices in 5 × 5 × 5 unit cell architectures with two different print paths using a rigid epoxy ink (Figure 3b). These print paths were generated with the semi-manual approach to have full control of the way struts are connected at the nodes. In Print Path 1, the lattice is printed in a piecewise fashion where lattice nodes are formed by printing ink traces side-by-side within a single lattice layer. In Print Path 2, the BCC lattice is printed in a diagonally piecewise fashion, where nodes in the lattice are ultimately formed by diagonally intersecting ink traces within a single layer of lattice unit cells. While different print paths result in visually similar lattices (Figure 3b), there are key differences in their node morphology (Figure 3c). Nodes formed via Print Path 1 possess less cohesive interfaces between contacting filaments within and between individual layers than those formed via Print Path 2. Such differences suggest that the mechanical integrity of the printed BCC lattices will be lower for Print Path 1. We determined the specific modulus, E/ρ, of each lattice from measurements of the compressive stress as a function of strain (Figure S10a, Supporting Information), which reveals that their print path design does impact mechanical performance (Figure 3d). Lattices printed with Print Paths 1 and 2 have $E_{PP1} = 1.02 \pm 0.20 \times 10^5$ Pa (kg^{-1} m^{-3}) and $E_{PP2} = 1.34 \pm 0.12 \times 10^5$ Pa (kg^{-1} m^{-3}), respectively.

Next, we explored the impact of print orientation on their mechanical properties. BCC lattices are printed with the rigid epoxy ink using Print Path 2 in 4 × 6 × 5 (orientation 1), 5 × 6 × 4 (orientation 2), and 6 × 5 × 4 (orientation 3) configurations. After printing, each lattice is rotated and mechanically characterized in a 4 × 6 × 5 orientation (Figure 3e). We anticipated that these lattices would be weaker under compressive loads in any orientation in which the loading direction would be parallel to the layers in which we must print the lattices. The compressive stress as a function of strain for the BCC lattices printed in the three orientations is provided in Figure S10b (Supporting

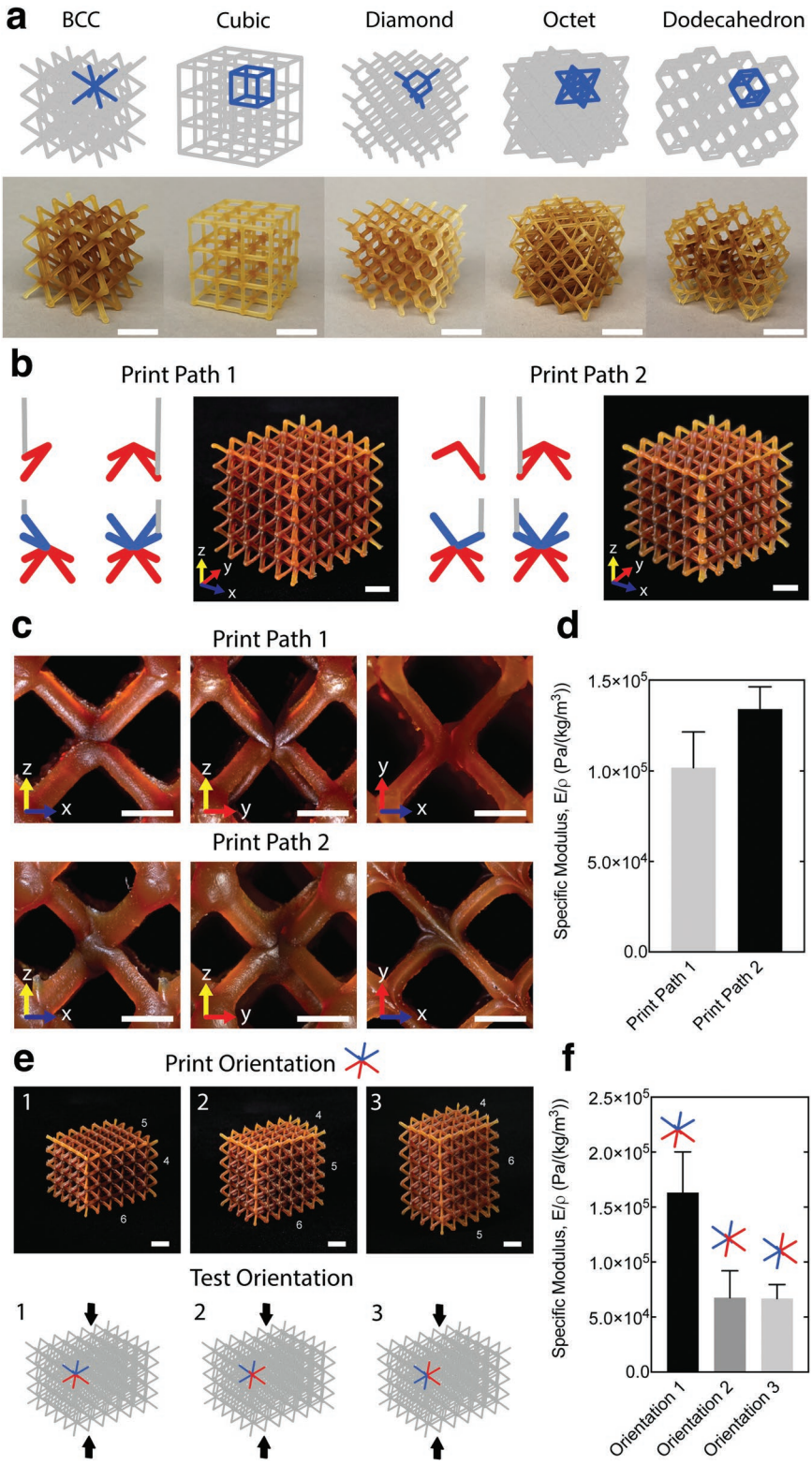

Figure 3. Periodic lattices. a) Printed epoxy lattices of varying geometry (scale bars = 10 mm). b) Two print paths used for EMB3D printing of a body-centered cubic (BCC) lattice (scale bars = 6 mm). c) Images of nodes from multiple orientations for each print path (scale bars = 3 mm). d) Specific modulus measured in the linear regime in stress-strain curves for 5 × 5 × 5 BCC lattices using each print path, n = 4. e) Lattices of the same size are printed in three orientations and rotated into the same configuration for compressive testing (scale bars = 6 mm). f) Specific modulus measured in the linear regime in stress-strain curves for each orientation printed with Print Path 2, n = 4.

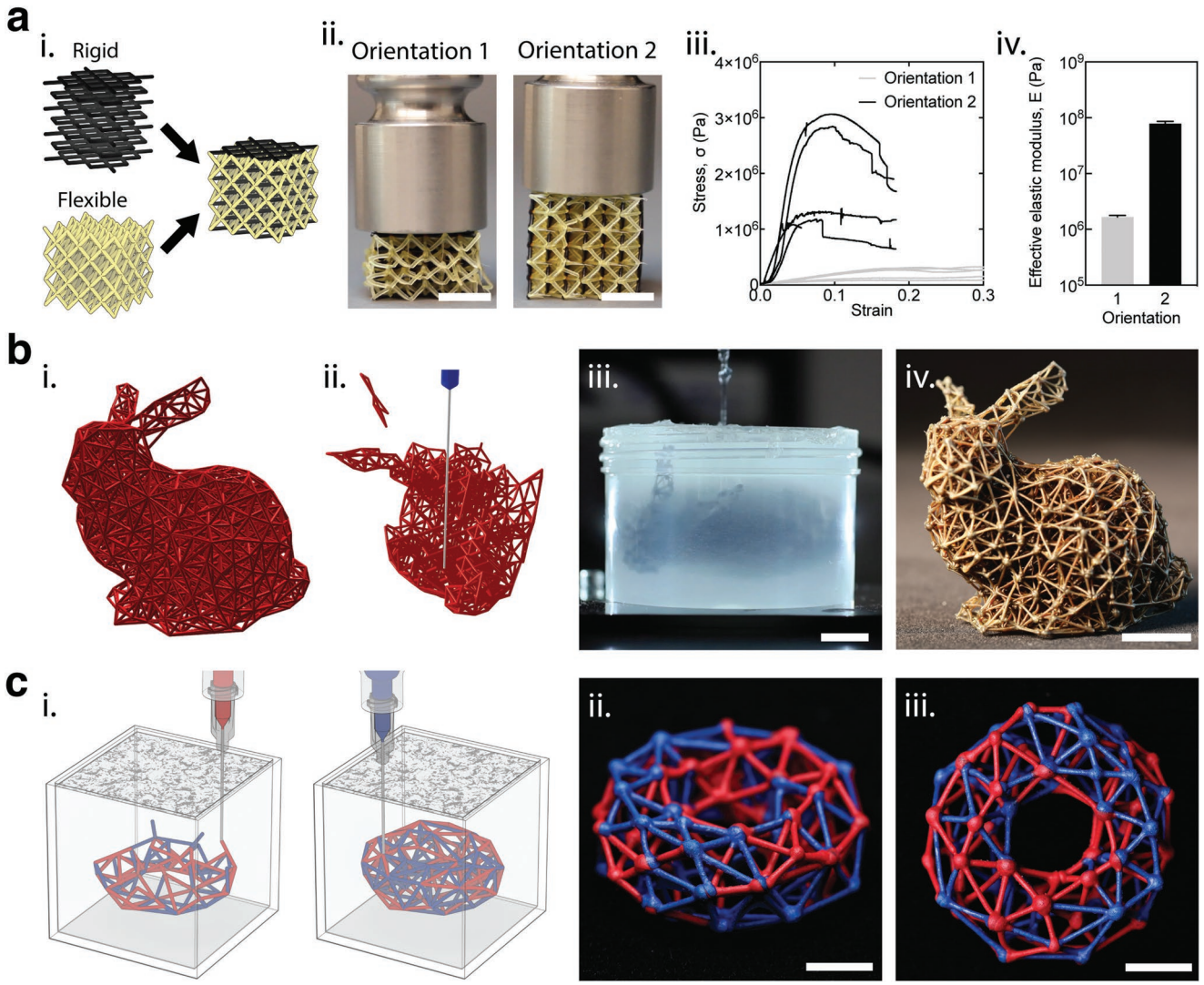

Figure 4. Multimaterial periodic and stochastic lattices. a) Schematic view of multi-material periodic lattice with programmed mechanical properties, which is composed of i) rigid and flexible struts and ii) exhibits different responses under compression for each orientation (scale bars = 10 mm). iii–iv) Stress-strain curves and the effective elastic moduli measured in the linear regime for these lattices oriented 0° and 90°, n = 5. b) Design and fabrication of a representative stochastic lattice based on the Stanford Bunny, where i) geometry creation, ii) print path planning using AERO, iii) EMB3D printing of the stochastic lattice (scale bars = 10 mm), and iv) image of printed lattice after curing and removal from the matrix (scale bar = 20 mm). c) Multimaterial stochastic torus lattice. i) Schematic view of multi-material stochastic lattice being printed using two independent printheads. ii–iii) Images of printed torus lattice composed of red- and blue-dyed epoxy struts and nodes (scale bars = 10 mm).

Information). Analysis of the specific modulus, defined as the elastic modulus per mass density (E/ρ), indicates that orientation 1 is the stiffest at $E_1/\rho_1 = (1.63 \pm 0.37) \times 10^5$ Pa (kg^{-1} m^{-3}), as expected, given that the loading direction is perpendicular to the interfaces between different layers in the lattice (Figure 3f). Within error, E/ρ for $5 \times 6 \times 4$ and $6 \times 5 \times 4$ lattices have similar values with $E_2/\rho_2 = (6.76 \pm 2.44) \times 10^4$ Pa (kg^{-1} m^{-3}) and $E_3/\rho_3 = (6.69 \pm 1.27) \times 10^4$ Pa/(kg/m^3), respectively. Hence, the print orientation directly impacts the structural integrity and mechanical properties of EMB3D printed lattices.

To generate more complex periodic lattices, we created a multi-material octet lattice consisting of rigid epoxy ink struts in the x-y plane and flexible epoxy ink struts in all other orientations (**Figure 4**a(i)). Two ink reservoirs with independently controlled z-axis motion are mounted alongside one another on the same x-y gantry. The nozzle through which ink is actively printed is lowered into the matrix, while the nozzle containing the other ink remains above the matrix. The resulting multimaterial lattices exhibit highly anisotropic mechanical properties, whereby their stiffness is nearly two orders of magnitude larger when a compressive load is parallel to the rigid plane of struts (Figure 4(ii-iv), Movie S10, Supporting Information). To highlight the power of AERO, we created a print path for a complex stochastic lattice based on Stanford bunny model,[82] a popular computer graphics 3D test model, consisting of 351 vertices and 1091 edges (Figure 4b(i)). The lattice is composed of an inner filled region with repeating BCC lattice cells connected to a stochastic lattice skin. The structure is designed

in Rhino3D using the algorithmic modeling tool Grasshopper, augmented by lattice design packages,[83,84] and exported as a graph to AERO to generate a print path (Figure 4b(ii), Movie S11, Supporting Information). Next, this complex lattice is printed (Figure 4b(iii), Movie S12 (Supporting Information) and post-processed. As a final demonstration, we combined AERO with multi-material EMB3D printing to fabricate a multi-material stochastic lattice by co-printing red and blue dyed epoxies (Figure 4c).

Importantly, our AERO algorithm can be applied to rapidly generate print paths for arbitrary strut-based structures for any 3D object with the singular goal of minimizing print time by optimizing the number of travel motions. In future embodiments, additional objectives could be incorporated to ensure that print time and mechanical properties are optimized. For example, print path generation could also take into account the ink and matrix rheology, which impact lattice node structure and mechanical behavior.[60] AERO operates in a segmented approach, as subgraphs of valid printable edges are determined and completely printed before the next subgraph is recalculated. This method could be upgraded to dynamically refresh the subgraph following each edge added to the print path which would enable a continuous path to overlap on itself, likely further reducing the number of travel motions required. Since the criteria for print path failure is well defined (i.e., when the nozzle crosses another printed filament), reinforcement learning may offer a promising alternative approach for optimizing EMB3D printing of complex architectures. Reinforcement learning (RL) is well suited for problems that require sequential decision-making,[85–87] such as determining the order in which to print struts. The reward for a RL-based printing path planning algorithm would be getting further into the print, simply measured as the number of struts successfully printed, and the penalty would be the time to complete the print and collisions of the nozzle with a filament. Both can be easily measured, such that the model could be trained in simulation. Beyond creating lattices for structural applications, AERO could be used to plan print paths for patterning sacrificial inks that template complex fluidic networks, e.g., pneumatic pathways for soft robots.[57,58] Looking ahead, by implementing a printing platform with a greater number of degrees of freedom (e.g., robotic arms with 6-axis control) coupled with switching nozzles[88,89] and generative design for topology optimization, more sophisticated structures could be generated using a single continuous print path.

In summary, EMB3D printing represents an enabling platform for creating architected lattices with spatially controlled geometry, composition, and mechanics. By harnessing graph-based print path planning via AERO, we have demonstrated that EMB3D printed lattices can be generated with a level of sophistication that exceeds other 3D printing methods by simultaneously integrating multiple materials with disparate properties. Our work opens new opportunities in the design and fabrication of architected matter for use in structural, metamaterial, and soft robotic applications.

3. Experimental Section

Lattice Design and Print Path Planning: Print paths used to print the BCC, cubic, diamond, octet, and dodecahedron lattices were generated in Python by individually studying the geometry of a single lattice unit cell and parameterizing the path needed to generate lattices of arbitrary size and cell count. The output of this script is the G-Code required to control the motion of the nozzle. As the lattice type becomes more complex or a stochastic lattice design is desired, this process of designing the print path was no longer tractable. To print lattices of arbitrary geometries, an algorithm using graph theory was developed, which we refer to as Automated Eulerian Route Optimization (AERO). Stochastic lattices were designed using Grasshopper, a programming interface for the CAD program Rhinoceros. Tools from the open-source plugins IntraLattice[83] and Crystallon[84] were used with custom tools to generate the lattice structures and export geometry in the form of a graph (collection of edges and vertices) for processing in AERO.

Epoxy Thermoset Inks: Thermoset inks were produced from two epoxy resins. The rigid ink was composed of a base epoxy resin (Epon 826, Hexion), a reactive diluent (dimethylmethyl phosphonate, DMMP, Millipore Sigma), a rheological modifier (fumed silica, CAB-O-SIL M5, Cabot), and a curing agent (Basionics VS03, BASF). To produce the rigid ink, 3 g DMMP and 2 g fumed silica were added to 30 g of Epon 826 resin. The components are mixed in a planetary mixer (FlackTeK SpeedMixer) at 800 rpm for 30 s, 1600 rpm for 30 s, and 2200 rpm for 3 min. Once the mixture had cooled to room temperature, 1.5 g of VS03 curing agent was added, and the mixing cycle was repeated. The flexible epoxy ink was prepared using the same base epoxy resin (Epon 826, Hexion) combined with a functional modifier to improve flexibility (Heloxy 505, Hexion), hexahydrophthalic anhydride (Millipore Sigma) as an epoxy hardener, fumed silica (CAB-O-SIL TS-720, Cabot) as a rheological modifier, and a curing agent (Epikure 3253, Hexion). To produce the flexible epoxy ink, 21 g Heloxy 505, 3 g hexahydrophthalic anhydride, and 3.75 g of fumed silica were added to 9 g of Epon 826 resin. The components were mixed using the same protocol as the rigid inks. The flexible epoxy ink was then cooled to room temperature prior to adding 0.45 g of the curing agent and the mixing cycle was repeated. Both inks are loaded into 10cc syringe barrels (Nordson EFD) and mixed at 3500 rpm for 7 min in a planetary mixer to remove any entrapped air. Inks used to explore the effects of rheology on printing behavior, which are slightly modified versions of the rigid epoxy ink, contain 10 g of Epon 826 resin, 0.5 g of Basionics VS03, 0.05 g of carbon black (added for visualization purposes) with varying amounts of TS-720 fumed silica (2.8 wt.%, 5.7 wt.%, 13.3 wt.%).

Rheological Characterization: The rheological behavior of the epoxy inks and matrix material were characterized using a controlled stress rheometer (Discovery HR-3, TA Instruments) equipped with a 40 mm parallel plate geometry with a 600 µm gap and sandpaper (60 Grit, McMASTER-CARR) affixed to both surfaces to prevent any secondary flows. Each ink and matrix material was separately loaded between the plates and trimmed using a spatula to produce a clean edge. Their apparent viscosity was measured using a logarithmic shear rate sweep from 0.01 1/s to 10 1/s. Their storage (G') and loss (G'') moduli are measured using an oscillatory sweep at a fixed 1 Hz frequency with the shear stress increasing from 1 Pa to 10 KPa. The yield stress for each fluid is defined as the shear stress at the crossover between G' and G''.

Embedded 3D Printing: Lattices were EMB3D printed using a custom multi-material 3D printer (ABG 10 000 gantry, Aerotech Inc., Pittsburg, PA, USA) and Python scripts for G-Code generation developed in-house. EMB3D printing began with loading the matrix material (DC9041, Dow-Corning) into a container (MAX 40, FlackTek). The container is carefully filled with the matrix to minimize the introduction of air cavities. The container was then centrifuged at 3000 RPM for 3 min, placed in a vacuum at -100 KPa for 2 min, and centrifuged once more at 3000 RPM for 3 min to remove any entrapped air. The container was fixed in place on the printer stage using a laser cut acrylic fixture. Inks were extruded through a commercially available 410 um inner diameter, 1.5″ long stainless-steel nozzle (Nordson EFD) at 85–95 PSI with a 1 mm s^{-1} nozzle translation speed. For smaller lattices, extrusion was controlled with air pressure using a digital pneumatic regulator (Ultimus V, EFD) connected to the motion controller (A3200, Aerotech) over serial. For the larger bunny lattice, a positive displacement pump (Vipro-HEAD 3, ViscoTec) was used to ensure consistent flow rate over the course of

a much longer print. The positive displacement pump was driven by a custom stepper driver board connected to a stepper controller (NSTEP, Aerotech) enabling synchronization between the volumetric flow rate and motion of the gantry. After printing, the container with the matrix material and embedded lattice was placed in a 100 °C oven overnight to cure. Once cured, the lattice was removed from the matrix, and any matrix material entrapped in the lattice was removed using pressurized air. The lattice was then left to soak overnight in hexanes to remove any remaining matrix material.

Mechanical Characterization: Prior to conducting mechanical tests, the loading faces of each lattice sample were sanded to render them flat and parallel to each other. To preserve their structural integrity, the lattices were removed from the matrix material, cleaned, and then embedded in prototyping wax (McMaster), which was subsequently melted and removed. All mechanical tests were carried out using an electromechanical testing system (Instron 5566). The compressive tests were carried out until failure using a 10 kN load cell at a rate of 0.005 mm s^{-1}. The stress values are calculated as the force exerted on the sample divided by the cross-sectional area of the entire structure (as defined by its outer envelope). Young's modulus is calculated as the slope of the stress-strain curve at 75% of the compressive strength using a custom MATLAB script. Finally, the specific modulus was calculated as the ratio between the measured Young's modulus and the lattice density, which is determined by the ratio between lattice mass and volume of the envelope.

Statistical Analysis: The specific modulus data from compressive testing is presented as the mean ± SD for sample size (n = 4) in each configuration (print path type and orientation). The effective elastic modulus for the multi-material octet lattice is presented as the mean ± SD for sample size (n = 5). Analyses were performed using GraphPad prism 9 for macOS (GraphPad Software).

Supporting Information

Supporting Information is available from the Wiley Online Library or from the author.

Acknowledgements

R.D.W. and R.L.T. contributed equally to this work. The authors acknowledge support from the NSF through Harvard Materials Research Science and Engineering Center Grant (MRSEC) DMR-1420570 and NSF Designing Materials to Revolutionize and Engineer our Future (DMREF-15-33985). J.A.L. also thanks GETTYLAB for their generous support of this work. Finally, the authors thank L. K. Sanders for assistance with photography and videography.

Conflict of Interest

The authors declare no conflict of interest.

Author Contributions

R.D.W, R.L.T., and J.A.L. designed research; R.D.W, R.L.T., S.G.M.U. performed research; all authors analyzed data; R.D.W, R.L.T., and J.A.L. wrote the paper.

Data Availability Statement

The data that support the findings of this study are available from the corresponding author upon reasonable request.

Keywords

embedded 3D printing, lattice, structural, multimaterial, print path planning

Received: July 31, 2022
Revised: November 12, 2022
Published online:

[1] T. A. Schaedler, W. B. Carter, *Annu. Rev. Mater. Res.* **2016**, *46*, 187.
[2] K. Bertoldi, V. Vitelli, J. Christensen, M. van Hecke, *Nat. Rev. Mater.* **2017**, *2*, 17066.
[3] J. Bauer, L. R. Meza, T. A. Schaedler, R. Schwaiger, X. Zheng, L. Valdevit, *Adv. Mater.* **2017**, *29*, 1701850.
[4] T. A. Schaedler, A. J. Jacobsen, A. Torrents, A. E. Sorensen, J. Lian, J. R. Greer, L. Valdevit, W. B. Carter, *Science* **2011**, *334*, 962.
[5] X. Zheng, H. Lee, T. H. Weisgraber, M. Shusteff, J. DeOtte, E. B. Duoss, J. D. Kuntz, M. M. Biener, Q. Ge, J. A. Jackson, S. O. Kucheyev, N. X. Fang, C. M. Spadaccini, *Science* **2014**, *344*, 1373.
[6] L. R. Meza, A. J. Zelhofer, N. Clarke, A. J. Mateos, D. M. Kochmann, J. R. Greer, *Proc. Natl. Acad. Sci. U. S. A.* **2015**, *112*, 11502.
[7] J. Bauer, A. Schroer, R. Schwaiger, O. Kraft, *Nat. Mater.* **2016**, *15*, 438.
[8] H. M. A. Kolken, A. A. Zadpoor, *RSC Adv.* **2017**, *7*, 5111.
[9] J. I. Lipton, R. MacCurdy, Z. Manchester, L. Chin, D. Cellucci, D. Rus, *Science* **2018**, *360*, 632.
[10] A. Ion, L. Wall, R. Kovacs, P. Baudisch, in *Proceedings of the 2017 CHI Conference on Human Factors in Computing Systems*, ACM, Denver Colorado USA, **2017**, pp. 977–988.
[11] J. R. Raney, B. G. Compton, J. Mueller, T. J. Ober, K. Shea, J. A. Lewis, *Proc. Natl. Acad. Sci. U. S. A.* **2018**, *115*, 1198.
[12] E. D. Sanders, A. Pereira, G. H. Paulino, *Sci. Adv.* **2021**, *7*, eabf4838.
[13] J. Mueller, J. A. Lewis, K. Bertoldi, *Adv Funct Materials* **2022**, *32*, 2105128.
[14] J. T. B. Overvelde, J. C. Weaver, C. Hoberman, K. Bertoldi, *Nature* **2017**, *541*, 347.
[15] B. Haghpanah, L. Salari-Sharif, P. Pourrajab, J. Hopkins, L. Valdevit, *Adv. Mater.* **2016**, *28*, 7915.
[16] J. Liu, T. Gu, S. Shan, S. H. Kang, J. C. Weaver, K. Bertoldi, *Adv. Mater.* **2016**, *28*, 6619.
[17] J. W. Boley, W. M. van Rees, C. Lissandrello, M. N. Horenstein, R. L. Truby, A. Kotikian, J. A. Lewis, L. Mahadevan, *Proc. Natl. Acad. Sci. U. S. A.* **2019**, *116*, 20856.
[18] X. Xia, A. Afshar, H. Yang, C. M. Portela, D. M. Kochmann, C. V. Di Leo, J. R. Greer, *Nature* **2019**, *573*, 205.
[19] Y. Jiang, L. M. Korpas, J. R. Raney, *Nat. Commun.* **2019**, *10*, 128.
[20] L. V. Elliott, E. E. Salzman, J. R. Greer, *Adv. Funct. Mater.* **2021**, *31*, 2008380.
[21] S. Shan, S. H. Kang, J. R. Raney, P. Wang, L. Fang, F. Candido, J. A. Lewis, K. Bertoldi, *Adv. Mater.* **2015**, *27*, 4296.
[22] J. R. Raney, N. Nadkarni, C. Daraio, D. M. Kochmann, J. A. Lewis, K. Bertoldi, *Proc. Natl. Acad. Sci. U. S. A.* **2016**, *113*, 9722.
[23] J. U. Surjadi, L. Gao, H. Du, X. Li, X. Xiong, N. X. Fang, Y. Lu, *Adv. Eng. Mater.* **2019**, *21*, 1800864.
[24] M. Pishvar, R. L. Harne, *Adv. Sci.* **2020**, *7*, 2001384.
[25] A. Rafsanjani, K. Bertoldi, A. R. Studart, *Sci. Robot.* **2019**, *4*, eaav7874.
[26] A. Clausen, F. Wang, J. S. Jensen, O. Sigmund, J. A. Lewis, *Adv. Mater.* **2015**, *27*, 5523.
[27] M. Osanov, J. K. Guest, *Annu. Rev. Mater. Res.* **2016**, *46*, 211.
[28] D. Chen, M. Skouras, B. Zhu, W. Matusik, *Sci. Adv.* **2018**, *4*, eaao7005.
[29] G. X. Gu, C.-T. Chen, D. J. Richmond, M. J. Buehler, *Mater. Horiz.* **2018**, *5*, 939.

[30] J. Z. Zhang, C. Sharpe, C. C. Seepersad, *J. Mech. Des.* **2020**, *142*, 091702.
[31] J. R. Raney, J. A. Lewis, *MRS Bull.* **2015**, *40*, 943.
[32] C. M. Spadaccini, *MRS Bull.* **2019**, *44*, 782.
[33] D. Chen, X. Zheng, *Sci. Rep.* **2018**, *8*, 9139.
[34] Z. C. Eckel, C. Zhou, J. H. Martin, A. J. Jacobsen, W. B. Carter, T. A. Schaedler, *Science* **2016**, *351*, 58.
[35] J. A. Jackson, M. C. Messner, N. A. Dudukovic, W. L. Smith, L. Bekker, B. Moran, A. M. Golobic, A. J. Pascall, E. B. Duoss, K. J. Loh, C. M. Spadaccini, *Sci. Adv.* **2018**, *4*, eaau6419.
[36] R. L. Truby, L. Chin, D. Rus, *IEEE Robot. Autom. Lett.* **2021**, *6*, 795.
[37] J. R. Tumbleston, D. Shirvanyants, N. Ermoshkin, R. Janusziewicz, A. R. Johnson, D. Kelly, K. Chen, R. Pinschmidt, J. P. Rolland, A. Ermoshkin, E. T. Samulski, J. M. DeSimone, *Science* **2015**, *347*, 1349.
[38] X. Zheng, W. Smith, J. Jackson, B. Moran, H. Cui, D. Chen, J. Ye, N. Fang, N. Rodriguez, T. Weisgraber, C. M. Spadaccini, *Nat. Mater.* **2016**, *15*, 1100.
[39] M. Schreck, N. Kleger, F. Matter, J. Kwon, E. Tervoort, K. Masania, A. R. Studart, M. Niederberger, *Small* **2021**, *17*, 2104089.
[40] L. R. Meza, S. Das, J. R. Greer, *Science* **2014**, *345*, 1322.
[41] C. Yan, L. Hao, A. Hussein, D. Raymont, *Int. J. Mach. Tools Manuf.* **2012**, *62*, 32.
[42] M. Leary, M. Mazur, J. Elambasseril, M. McMillan, T. Chirent, Y. Sun, M. Qian, M. Easton, M. Brandt, *Mater. Des.* **2016**, *98*, 344.
[43] L. Liu, P. Kamm, F. García-Moreno, J. Banhart, D. Pasini, *J. Mech. Phys. Solids* **2017**, *107*, 160.
[44] S. Yuan, F. Shen, J. Bai, C. K. Chua, J. Wei, K. Zhou, *Mater. Des.* **2017**, *120*, 317.
[45] S. Yuan, C. K. Chua, K. Zhou, *Adv. Mater. Technol.* **2019**, *4*, 1800419.
[46] B. C. White, A. Garland, R. Alberdi, B. L. Boyce, *Addit. Manuf.* **2021**, *38*, 101741.
[47] J. J. Martin, B. E. Fiore, R. M. Erb, *Nat. Commun.* **2015**, *6*, 8641.
[48] J. T. Muth, P. G. Dixon, L. Woish, L. J. Gibson, J. A. Lewis, *Proc. Natl. Acad. Sci. U. S. A.* **2017**, *114*, 1832.
[49] B. Román-Manso, J. Muth, L. J. Gibson, W. Ruettinger, J. A. Lewis, *ACS Appl. Mater. Interfaces* **2021**, *13*, 8976.
[50] B. G. Compton, J. A. Lewis, *Adv. Mater.* **2014**, *26*, 5930.
[51] J. Mueller, J. R. Raney, K. Shea, J. A. Lewis, *Adv. Mater.* **2018**, *30*, 1705001.
[52] R. D. Farahani, M. Dubé, D. Therriault, *Adv. Mater.* **2016**, *28*, 5794.
[53] W. Wu, A. DeConinck, J. A. Lewis, *Adv. Mater.* **2011**, *23*, H178.
[54] J. T. Muth, D. M. Vogt, R. L. Truby, Y. Mengüç, D. B. Kolesky, R. J. Wood, J. A. Lewis, *Adv. Mater.* **2014**, *26*, 6307.
[55] T. J. Hinton, Q. Jallerat, R. N. Palchesko, J. H. Park, M. S. Grodzicki, H.-J. Shue, M. H. Ramadan, A. R. Hudson, A. W. Feinberg, *Sci. Adv.* **2015**, *1*, e1500758.
[56] T. Bhattacharjee, S. M. Zehnder, K. G. Rowe, S. Jain, R. M. Nixon, W. G. Sawyer, T. E. Angelini, *Sci. Adv.* **2015**, *1*, e1500655.
[57] M. Wehner, R. L. Truby, D. J. Fitzgerald, B. Mosadegh, G. M. Whitesides, J. A. Lewis, R. J. Wood, *Nature* **2016**, *536*, 451.
[58] R. L. Truby, M. Wehner, A. K. Grosskopf, D. M. Vogt, S. G. M. Uzel, R. J. Wood, J. A. Lewis, *Adv. Mater.* **2018**, *30*, 1706383.
[59] M. A. Skylar-Scott, S. G. M. Uzel, L. L. Nam, J. H. Ahrens, R. L. Truby, S. Damaraju, J. A. Lewis, *Sci. Adv.* **2019**, *5*, eaaw2459.
[60] A. K. Grosskopf, R. L. Truby, H. Kim, A. Perazzo, J. A. Lewis, H. A. Stone, *ACS Appl. Mater. Interfaces* **2018**, *10*, 23353.
[61] E. Mirdamadi, J. W. Tashman, D. J. Shiwarski, R. N. Palchesko, A. W. Feinberg, *ACS Biomater. Sci. Eng.* **2020**, *6*, 6453.
[62] T. J. Hinton, A. Hudson, K. Pusch, A. Lee, A. W. Feinberg, *ACS Biomater. Sci. Eng.* **2016**, *2*, 1781.
[63] C. S. O'Bryan, T. Bhattacharjee, S. Hart, C. P. Kabb, K. D. Schulze, I. Chilakala, B. S. Sumerlin, W. G. Sawyer, T. E. Angelini, *Sci. Adv.* **2017**, *3*, e1602800.
[64] A. M. Compaan, K. Song, Y. Huang, *ACS Appl. Mater. Interfaces* **2019**, *11*, 5714.
[65] S. Shin, H. Kwak, D. Shin, J. Hyun, *Nat. Commun.* **2019**, *10*, 4650.
[66] T. Bhattacharjee, C. J. Gil, S. L. Marshall, J. M. Urueña, C. S. O'Bryan, M. Carstens, B. Keselowsky, G. D. Palmer, S. Ghivizzani, C. P. Gibbs, W. G. Sawyer, T. E. Angelini, *ACS Biomater. Sci. Eng.* **2016**, *2*, 1787.
[67] C. B. Highley, C. B. Rodell, J. A. Burdick, *Adv. Mater.* **2015**, *27*, 5075.
[68] Y. Jin, A. Compaan, W. Chai, Y. Huang, *ACS Appl. Mater. Interfaces* **2017**, *9*, 20057.
[69] C. B. Highley, K. H. Song, A. C. Daly, J. A. Burdick, *Adv. Sci.* **2019**, *6*, 1801076.
[70] A. Lee, A. R. Hudson, D. J. Shiwarski, J. W. Tashman, T. J. Hinton, S. Yerneni, J. M. Bliley, P. G. Campbell, A. W. Feinberg, *Science* **2019**, *365*, 482.
[71] N. Noor, A. Shapira, R. Edri, I. Gal, L. Wertheim, T. Dvir, *Adv. Sci.* **2019**, *6*, 1900344.
[72] Y. Zhang, S. T. Ellison, S. Duraivel, C. D. Morley, C. R. Taylor, T. E. Angelini, *Int. J. Bioprint.* **2021**, *21*, e00121.
[73] R. J. Trudeau, *Introduction to Graph Theory*, Dover Publications, New York, **1994**.
[74] Fleury, Pierre-Henry, *Journal de mathématiques élémentaires* **1883**, *2*, 257.
[75] C. S. O'Bryan, T. Bhattacharjee, S. R. Niemi, S. Balachandar, N. Baldwin, S. T. Ellison, C. R. Taylor, W. G. Sawyer, T. E. Angelini, *MRS Bull.* **2017**, *42*, 571.
[76] L. M. Friedrich, R. T. Gunther, J. E. Seppala, *ACS Appl. Mater. Interfaces* **2022**, *14*, 32561.
[77] L. M. Friedrich, J. E. Seppala, *Soft Matter* **2021**, *17*, 8027.
[78] J. Mueller, K. Shea, C. Daraio, *Mater. Des.* **2015**, *86*, 902.
[79] J. Mueller, K. Shea, *Mater. Today Commun.* **2018**, *17*, 69.
[80] D. J. McGregor, S. Tawfick, W. P. King, *Addit. Manuf.* **2019**, *25*, 10.
[81] M. Munford, U. Hossain, S. Ghouse, J. R. T. Jeffers, *Addit. Manuf.* **2020**, *32*, 101041.
[82] G. Turk, M. Levoy, in *Proceedings of the 21st Annual Conference on Computer Graphics and Interactive Techniques – SIGGRAPH '94*, ACM Press, Not Known, **1994**, pp. 311–318.
[83] "IntraLattice: Generative Lattice Design with Grasshopper," https://github.com/dnkrtz/intralattice,(accessed: October 2018).
[84] "Crystallon: Open source project for creating lattice structures," https://github.com/fequalsf/Crystallon, (accessed: October 2018).
[85] D. Silver, A. Huang, C. J. Maddison, A. Guez, L. Sifre, G. van den Driessche, J. Schrittwieser, I. Antonoglou, V. Panneershelvam, M. Lanctot, S. Dieleman, D. Grewe, J. Nham, N. Kalchbrenner, I. Sutskever, T. Lillicrap, M. Leach, K. Kavukcuoglu, T. Graepel, D. Hassabis, *Nature* **2016**, *529*, 484.
[86] A. Ecoffet, J. Huizinga, J. Lehman, K. O. Stanley, J. Clune, *Nature* **2021**, *590*, 580.
[87] D. Silver, T. Hubert, J. Schrittwieser, I. Antonoglou, M. Lai, A. Guez, M. Lanctot, L. Sifre, D. Kumaran, T. Graepel, T. Lillicrap, K. Simonyan, D. Hassabis, *Science* **2018**, *362*, 1140.
[88] J. O. Hardin, T. J. Ober, A. D. Valentine, J. A. Lewis, *Adv. Mater.* **2015**, *27*, 3279.
[89] M. A. Skylar-Scott, J. Mueller, C. W. Visser, J. A. Lewis, *Nature* **2019**, *575*, 330.